The Impact of Different Hydrogen Configurations on Light- and Elevated-Temperature-Induced Degradation

Benjamin Hammann, Nicole Assmann, Philip M. Weiser, Wolfram Kwapil, Tim Niewelt, Florian Schindler, Rune Søndenå, Eduard V. Monakhov, and Martin C. Schubert

***Abstract*—In this article, the impact of different hydrogen configurations and their evolution on the extent and kinetics of light- and elevated-temperature-induced degradation (LeTID) is investigated in float-zone silicon via charge carrier lifetime measurements, low-temperature Fourier-transform infrared spectroscopy, and four-point-probe resistance measurements. Degradation conditions were light soaking at 77 °C and 1 sun-equivalent illumination intensity and dark anneal at 175 °C. The initial configuration of hydrogen is manipulated by varying the wafer thickness, the cooling ramp of the fast-firing process, and the dopant type (B- or P-doped). We find lower hydrogen concentrations in thinner samples and samples with a slower cooling ramp. This suggests that hydrogen diffuses out of the sample during the cool-down, which strongly affects the final concentration of hydrogen molecules H_2, and to a smaller degree the concentration of boron-hydrogen (BH) pairs. A regeneration of potential LeTID defects and a presumed LeTID degradation during dark annealing is found in n-type Si. In p-type Si, the LeTID extent was found to scale with H_2, suggesting a direct link between both. The temporal evolution of BH pairs, LeTID degradation/regeneration, and surface degradation depends on wafer thickness and the cooling ramp of the fast-firing process. Based upon these findings, we formulate a theory of the hydrogen-related mechanism behind LeTID: Hydrogen originating from H_2 moves between different temporary traps. First, hydrogen binds to LeTID precursors and acceptor atoms in the silicon bulk, later moving toward the surface. This leads first to the LeTID degradation and regeneration and then to the degradation of surface passivation.**

***Index Terms*—Boron-hydrogen (BH) pairs, hydrogen, light- and elevated-temperature-induced degradation (LeTID), long-term stability, photovoltaics, silicon.**

Manuscript received 30 September 2022; revised 22 November 2022; accepted 3 January 2023. Date of publication 30 January 2023; date of current version 20 February 2023. The work of Benjamin Hammann was supported by "Stiftung Nagelschneider." This work was supported in part by the German Federal Ministry for Economic Affairs and Climate Action under Contract 03EE1052B and Contract 03EE1052D, in part by the Research Council of Norway through the Norwegian Research Centre for Sustainable Solar Cell Technology under Contract 257639, and in part by the Norwegian Microfabrication and Nanofabrication Facility, NorFab, under Project 295864. *(Corresponding author: Benjamin Hammann.)*

Benjamin Hammann, Florian Schindler, and Martin C. Schubert are with the Fraunhofer Institute for Solar Energy Systems ISE, 79110 Freiburg, Germany (e-mail: benjamin.hammann@ise.fraunhofer.de; florian.schindler@ise.fraunhofer.de; martin.schubert@ise.fraunhofer.de).

Nicole Assmann, Philip M. Weiser, and Eduard V. Monakhov are with the University of Oslo, 0315 Oslo, Norway (e-mail: nicole.assmann@smn.uio.no; pmw250@gmail.com; eduard.monakhov@fys.uio.no).

Wolfram Kwapil is with the Fraunhofer Institute for Solar Energy Systems ISE, 79110 Freiburg, Germany, and also with the Department of Sustainable Systems Engineering (INATECH), University of Freiburg, 79110 Freiburg, Germany (e-mail: wolfram.kwapil@ise.fraunhofer.de).

Tim Niewelt is with the Fraunhofer Institute for Solar Energy Systems ISE, 79110 Freiburg, Germany, also with the Department of Sustainable Systems Engineering (INATECH), University of Freiburg, 79110 Freiburg, Germany, and also with the School of Engineering, University of Warwick, Coventry CV4 7AL, U.K. (e-mail: tim.niewelt@ise.fraunhofer.de).

Rune Søndenå is with the Institute for Energy Technology, 2007 Kjeller, Norway (e-mail: rune.sondena@ife.no).

Color versions of one or more figures in this article are available at https://doi.org/10.1109/JPHOTOV.2023.3236185.

Digital Object Identifier 10.1109/JPHOTOV.2023.3236185

I. Introduction

HYDROGEN is one of the key elements for silicon solar cells. Its ability to passivate defects made it especially useful for stands for passivated emitter and rear cell (PERC) solar cells based on multicrystalline silicon, which benefited greatly from the passivation of interfaces and bulk with hydrogen [1], [2]. Furthermore, hydrogen has been demonstrated to play a role in the passivation of the boron-oxygen defect responsible for the light-induced degradation of boron-doped Czochralski-grown silicon [3], [4].

In light of those benefits, processes that facilitate the introduction of hydrogen have been used extensively in solar cell production. However, in 2012, a new degradation phenomenon was reported by Ramspeck et al. [5], which was later linked to the presence of hydrogen [6], [7], [8]. Because of its occurrence under illumination and at higher temperatures, this degradation phenomenon was termed light- and elevated-temperature-induced degradation (LeTID) [9]. It was found that LeTID can reduce the efficiency of solar cells in the field within years by up to 10%$_{\mathrm{rel}}$ [9]. Because of this negative impact, it is considered one of the most urgent problems to solve within the field of silicon solar cells [10]. Since hydrogenation of silicon solar cells still plays an important role for the passivation of defects and the surface [10], [11], hydrogen is still needed in modern solar cells. The key process is the fast-firing step, which is usually the final step in the solar cell production. Its main objective is to establish the contact between the usually printed metal fingers and busbars with the silicon underneath the passivation layers. A side effect of this fast-firing process is the release of hydrogen from the passivation layers into the silicon bulk. This gives rise to both its beneficial and detrimental effects. Different ways of manipulating the in-diffusion of hydrogen (and thus the LeTID extent) were hypothesized, notably by varying the cooling ramp of the fast-firing process [12] and the wafer thickness [13].

This work is licensed under a Creative Commons Attribution 4.0 License. For more information, see https://creativecommons.org/licenses/by/4.0/

Based on these concepts, this study investigates the influence of the cooling ramp and the wafer thickness on the initial hydrogen configuration. Further, we examine its impact on the extent and kinetics of LeTID in p- and n-type float-zone (FZ) silicon as well as on the kinetics of dominant hydrogen complexes, and thus gain a deeper understanding on the mechanism behind LeTID, needed for its optimal mitigation.

A. Light- and Elevated-Temperature-Induced Degradation

One crucial feature of LeTID is that it can appear independently of the material, e.g., in mc-Si [5], [9], cast-mono-Si [14], Cz-Si [15], or FZ-Si [16], [17]. Choosing another dopant than boron does also not prevent LeTID, as it was found in P-doped n-type [18] and Ga-doped p-type Si [5], [19] as well. LeTID itself can be triggered by illumination at elevated temperatures, as its naming suggests, but also by annealing in the dark, at comparably higher temperatures.

Independent of the treatment condition, the LeTID degradation is always followed by a regeneration, where the defect becomes recombination-inactive. Many authors additionally reported a degradation of the surface passivation that follows the (bulk-related) LeTID regeneration [20], [21], [22], [23], which we also observe in this study.

The extent of LeTID can be manipulated by different factors, like the peak temperature of the firing step [15], [24], the cooling ramp of the firing step [12], [25], different preannealing steps [26], [27], [28], but also sample properties like the composition of the silicon nitride layer [7], [29], [30], interlayers such as aluminum oxide (Al_2O_3) [31], [32], or the thickness of a sample [13], [33]. It was shown that the initial hydrogen concentration correlates with the peak firing temperature [34], besides other factors like the composition of the hydrogen-containing dielectric surface layers [35], or interlayers such as Al_2O_3 [32], [36]. The mechanism in which way cooling ramps, wafer thickness, and annealing conditions affect LeTID has not been revealed up to now.

B. Hydrogen

While there is general agreement that the presence of hydrogen is the main driver for the occurrence of LeTID, the physical background of LeTID is still unknown [6], [34], [37]. Within this study, we extend upon our previous work [37] on synchronized investigations of hydrogen and LeTID kinetics with improved characterization methods (see Section II for more details).

Hydrogen in silicon has been a research topic for many decades. In its atomic form, hydrogen can have different charge states (H^+, H^0, H^-) depending on the position of the Fermi level, which is impacted mainly by the doping concentration, the temperature, and the excess charge carrier density. Being a negative-U impurity defect, H^+ is dominant in p-type and H^- in n-type Si, whereas H^0 exists in relevant quantities only under certain conditions [38], [39].

Typical concentrations of hydrogen in the Si bulk, especially after solar cell-like processing, are orders of magnitude below the detection limit of secondary ion mass spectroscopy measurements, which is often used to detect elements with low concentrations. Therefore, other ways of investigating the properties of hydrogen have to be used. One characteristic of hydrogen is its ability to readily bind to dopants, especially to acceptors like B or Ga. This feature has often been used to study hydrogen kinetics by observing changes in active dopant concentrations [40], [41], [42], [43], [44], [45], [46]. While these techniques are always indirect because of their assumption that all observed changes in hole concentration relate to the formation of dopant-hydrogen complexes, optical measurements allow a more direct measurement of complex-related quantities. Raman scattering [47] or Fourier-transform infrared (FT-IR) spectroscopy [48], [49] are prominent examples of measurement techniques that are able to detect dopant-hydrogen complexes, but also other hydrogen-related complexes such as hydrogen molecules [48].

Based upon experimental findings, Voronkov and Falster [50] developed a theory on the kinetics of hydrogen that was extended by Hamer et al. [51], with the addition of a possible LeTID reaction later by Kwapil et al. [52].

Within the context of this study (1 Ωcm samples), these theories predict for B-doped, p-type Si that during the firing step at high temperatures most of the hydrogen is in atomic form. During the cooling phase, hydrogen binds to boron to form boron-hydrogen (BH) pairs and forms molecules H_2 (termed H_{2A} by Voronkov). At 1 Ωcm, after firing, most of the hydrogen exists in the molecular form with only a fraction being present as BH pairs.

According to this model, hydrogen molecules dissociate during dark annealing (DA) by capturing a hole, and the dissociated atomic hydrogen then binds to boron. Upon prolonged DA, the concentration of BH pairs decreases again, as observed in [53] and [48], and in recent publications such as [45], [46], and [54]. The following equations describe the expected reactions:

$$H_2 + h^+ \rightleftharpoons H^+ + H^0 \tag{1}$$

$$H^+ + B^- \rightleftharpoons BH \tag{2}$$

$$BH \rightleftharpoons X. \tag{3}$$

Until now, it is unclear what happens with the hydrogen after it dissociates from BH (3). Voronkov and Falster [50] presumed that it might form a second stable molecule, named H_{2C}, which, however, has not been experimentally detected. Based upon the findings in this study, we suggest that hydrogen diffuses toward the surface rather than being transformed in a different molecule configuration, leading to the observed reduction in BH. However, it is yet unclear what hydrogen sink might elicit this diffusion.

C. Design of Experiment

Within this study, we investigate how the cooling ramp and wafer thickness affect the hydrogen configuration in p- and n-type Si by measuring the concentration of hydrogen molecules (H_2) and BH pairs with low-temperature FT-IR spectroscopy. A special sample design is used to measure the effective lifetime

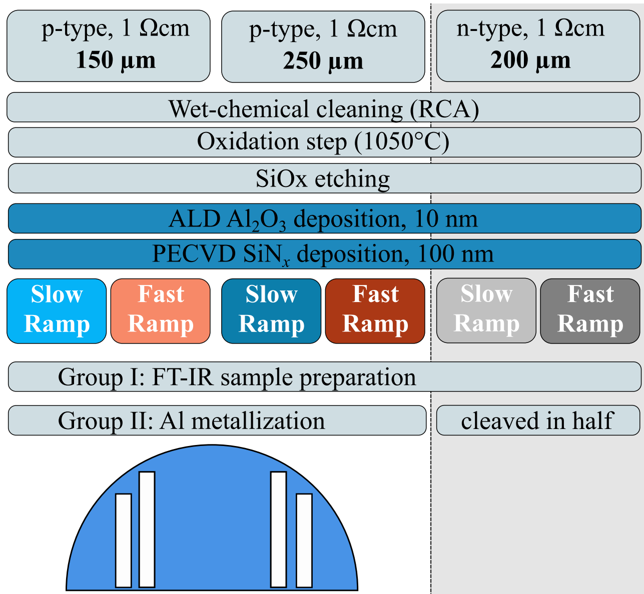

Fig. 1. Diagram showing the sample preparation process and, at the bottom, a schematic depiction of the metalized samples from Group II.

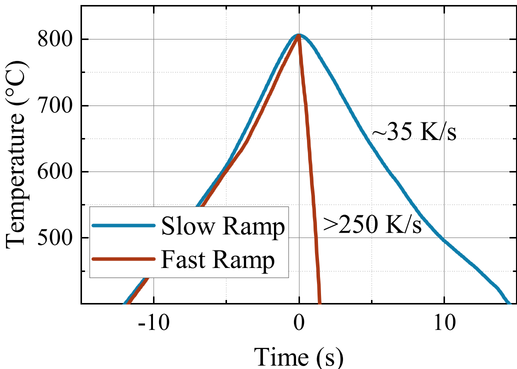

Fig. 2. Measured sample temperature during the two firing processes used within this experiment. Both feature a similar heating ramp up until 800 °C. Afterward, the cooling ramp is around 35 K/s (slow ramp) and >250 K/s (fast ramp).

and bulk resistivity of the samples. From these data, the kinetics of LeTID and of hydrogen are extracted under light soaking (LS) (77 °C, 1 sun-equivalent) and DA conditions (175 °C).

The combined information on hydrogen and LeTID gives indications on the relative impact of different H complexes for the formation of LeTID and on the role of hydrogen within the LeTID degradation-regeneration cycle. We additionally investigate how hydrogen and the surface degradation are linked, as well as bulk-related degradation-regeneration phenomena observed in n-type wafers.

II. Experimental Methods

A. Sample Preparation

In this study, 4″ diameter FZ silicon wafers with a bulk resistivity of 1 Ωcm are used. Boron-doped p-type wafers with two different thicknesses, 150 and 250 µm, and 200-µm-thick phosphorus-doped n-type wafers are processed as shown in Fig. 1: First, the wafers are cleaned using an adapted RCA cleaning sequence, followed by an oxidation treatment performed at 1050 °C for 60 min in order to remove any residual hydrogen that is sometimes found in bare FZ-Si wafers [45]. It also prevents the formation of a defect that typically occurs in FZ-Si during processes in the temperature range between 400 °C and 800 °C [55]. The grown silicon oxide is etched off, and the wafer surfaces are passivated symmetrically using a stack of 10 nm thin Al_2O_3 and a 100-nm-thick hydrogenated silicon nitride layer (SiN_x:H), with a standard refractive index of 2.01. The Al_2O_3 deposition is done using atomic layer deposition at around 230 °C, whereas the SiN_x:H is deposited using plasma-enhanced chemical vapor deposition at around 400 °C.

The subsequent firing step then introduces the hydrogen from the SiN_x:H into the silicon bulk, which is achieved using two different firing profiles, as shown in Fig. 2.

The important distinguishing feature is the cooling ramp that is 35 K/s for the slow ramp and >250 K/s for the fast ramp. The slow ramp is achieved in a conventional industrial belt furnace, whereas the fast process is conducted in an offline rapid thermal processing (RTP) oven. In this offline RTP oven, the samples are heated using a laser with 980 nm wavelength. The high cooling rate is achieved by additional air-cooling. For more details on the offline RTP tool, the reader is referred to [56]. It is important to note that temperature profiles are measured with thermocouples, and additional care was taken to obtain the same temperature profile independent of wafer thickness. Note that typical industrial cooling ramps usually range in between the two cases investigated here.

Afterward, samples of Group I (see Fig. 1) are prepared for FT-IR measurements, which are described in more detail in the following. The rest of the samples (Group II) are cleaved in half. The p-type samples are metalized with four aluminum stripes on the front side, using a laser metal bonding method [57]. This has the advantage of heating the sample only locally on the contacts, which is important to prevent influences on the overall hydrogen configuration. The sample design is schematically shown in Fig. 1 and based on the design from [58]. These four aluminum contacts are used to conduct four-point-probe (4PP) measurements, whereas in the sample center, enough space is provided (>40 × 40 mm^2) to measure effective lifetime (for details on 4PP and lifetime measurements, the reader is referred to the following sections).

B. Low-Temperature FT-IR Measurements

For FT-IR measurements, specific samples undergo a fabrication process and are then stacked based on the concept described in [49]. First, the passivation stack Al_2O_3/SiN_x is etched off by dipping in 10% hydrofluoric acid for ∼15 min. Then, using a specially developed laser-based process, the half wafers are cleaved into small 10 × 10 mm^2 squares. Stacking the tokens results in a cuboid of around 10 × 10 × 5 mm^3, schematically depicted in Fig. 3. Since a long path length is needed to detect H_2 molecules [48], this design allows for an absorption path of 10 mm while also minimizing reflection losses.

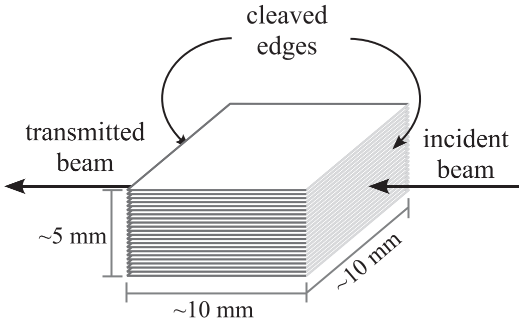

Fig. 3. Schematic depiction of the sample stack used for FT-IR measurements. The beam enters and leaves the stack through the specially cleaved sides.

The FT-IR measurements are performed in a Bruker IFS 125HR spectrometer at 5 K, equipped with a globar source and a KBr beam splitter in the mid-infrared range. The vibrational lines of BH pairs at 1904 cm^{-1} and H_2 molecules at 3618.4 cm^{-1} are used to calculate the respective concentrations using the calibration coefficients $A_{BH} = (3.0 \pm 0.3)\cdot 10^{15}$ cm^{-1} [59] and $A_{H2} = (8.0 \pm 0.1)\cdot 10^{17}$ cm^{-1} [60], respectively.

C. Measurement of Changes in BH Pairs by Resistivity Measurements

For 4PP resistivity measurements, the samples are placed on a copper stage with constant temperature kept at (25.00 ± 0.05) °C using Peltier elements. The samples are electrically contacted using needles, which also press the sample to the copper stage to ensure a good thermal contact. The probes are connected to a Keithley 2002 DMM for four-point resistance measurements. Care was taken that no current flows through the measurement stage.

To calculate the bulk resistivity ρ_{bulk} from the measured resistivity *R*, it is important to know the geometrical factor *f* of the sample that depends on the circuit geometry. The geometrical factor for the sample and setup geometry used in this study is calculated as $f = 1.045$ using Quokka3 [61], [62]. Together with the sample thickness *d*, the bulk resistivity can be calculated according to

$$\rho_{\text{bulk}} = R \cdot d / f. \tag{4}$$

Using the bulk resistivity, the change in BH pairs $\Delta[\text{BH}]_{4\text{PP}}$ can be calculated as explained, for example, in [44] or [58]. Combined with FT-IR measurements of initial [BH], the total BH-concentration is calculated via

$$[\text{BH}] = [\text{BH}]_{\text{FTIR}} + \Delta[\text{BH}]_{4\text{PP}}. \tag{5}$$

According to our investigations (data not shown here), this measurement procedure is highly reproducible within 0.1% of ρ_{bulk}. In accordance with the uncertainty analysis in [58], the uncertainty in calculated changes in [BH] is dominated by the reproducibility and we estimated it for the used 1 Ωcm p-type material to $\leq 1.5\cdot 10^{13}$ cm^{-3}. This is roughly one order of magnitude better than the eddy-current-based method employed previously [37], [44].

D. Assessment of Defect Density

Monitoring the effective lifetime during different treatment conditions allows us to track changes induced by LeTID and surface related degradation (SRD). The effective lifetime is measured in multiple ways: First, the effective lifetime is measured as a function of excess carrier density $\tau_{\text{eff}}(\Delta n)$ using the photoconductance decay (PCD) method with a WCT-120 Sinton Lifetime Tester [63] with both a short and long flash. Second, photoluminescence (PL) lifetime images at 1 and 0.05 sun equivalents calibrated by modulated PL [64] are taken.

Since some of the p-type wafers show inhomogeneous lifetime distributions, their PCD measurements were unreliable, probably because of small displacement changes in relation to the WCT-120's sensitivity region. Because of this, all p-type wafers are evaluated using the PL lifetime images with the following procedure.

For every p-type sample, the PL images obtained at 0.05 sun-equivalent throughout a degradation treatment are aligned and a homogenous spot is chosen. A mean $\tau(\Delta n)$-value of the chosen spot is calculated using a harmonic mean. With $\tau(\Delta n)$, it is possible to calculate lifetime-equivalent changes in defect density ΔN according to

$$\Delta N = \frac{1}{\tau(t)} - \frac{1}{\tau_0} \tag{6}$$

where $\tau(t)$ represents the lifetime at a treatment time *t*, and τ_0 the measured effective lifetime before the treatment [65]. This quantity is used to describe the temporal evolution of LeTID. Since PL-lifetime images are obtained at constant generation (0.05 sun-equivalent), changes in a lifetime will also impact the reached excess carrier density. To account for different Δn-values, the parameterization of a relative defect density β is used to compare the maximum LeTID extent, as suggested by Kim et al. [66]

$$\beta_{\max} \approx \left(\frac{\Delta n}{N_{\text{dop}} + \Delta n} \cdot \frac{k}{v_{\text{th,p}}} + \frac{1}{v_{\text{th,n}}} \right) \cdot \Delta N \tag{7}$$

with the doping concentration N_{dop}, the thermal velocity of electron (holes) $v_{\text{th,n}}$ ($v_{\text{th,p}}$), and the ratio of the electron and hole capture cross section *k*. Under the assumption that changes in ΔN are because of LeTID defects, *k* is set to a typical value for LeTID of $k = 35$ (refer to [67] for an overview of determined *k*-factors).

III. Results and Discussion

In the first step, the different hydrogen configurations are investigated with low-temperature FT-IR measurements (Section III-A). Then, the influence of those different configurations on the extent of LeTID in p-type samples is investigated in Section III-B. The kinetics of LeTID and their relation to hydrogen are discussed in Sections III-C and III-D. Lastly, the impact on LeTID in n-type samples is discussed in Section III-E.

A. Manipulating the Hydrogen Configuration

Samples from group I (see Fig. 1) are measured with low-temperature FT-IR spectroscopy to detect the local vibration

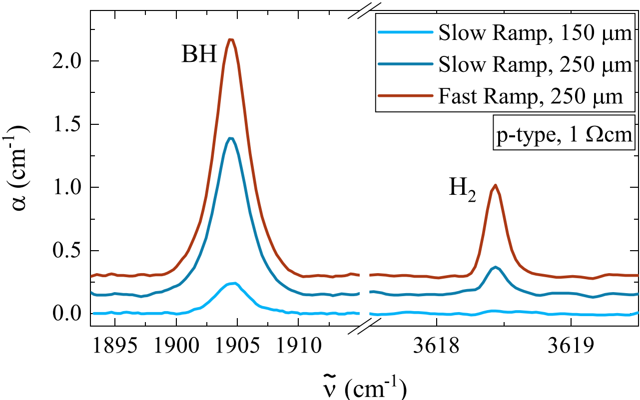

Fig. 4. IR absorption coefficient spectra of p-type samples obtained at 5.0 K. Samples with different cooling and wafer thicknesses are depicted. The LVMs of BH at 1904 cm^{-1} and H_2 at 3618.4 cm^{-1} are shown. The spectra are vertically offset for clarity.

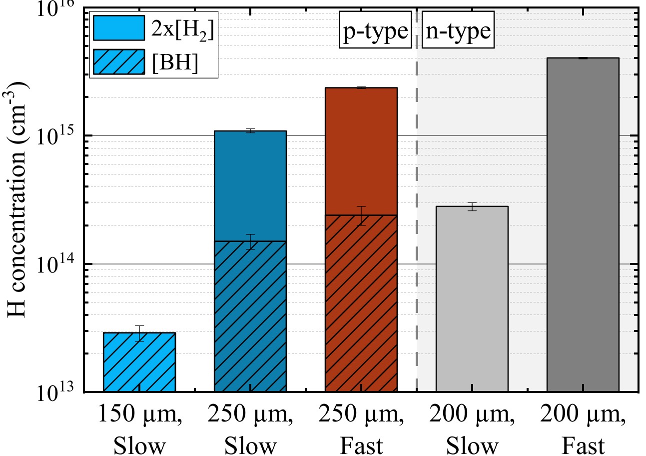

Fig. 5. Concentration of atomic hydrogen present in H_2 molecules and BH-pairs measured with FTIR at 5.0 K. Samples differ in the doping type (p: left/n: right), the wafer thickness (150/200/250 µm), and the cooling ramp of the firing process (slow/fast). BH concentration is shown by hatched bars. The maximum value of each bar represents the total concentration of hydrogen (i.e., [BH] + 2×[H_2]).

modes (LVMs) of BH pairs and H_2 molecules. Exemplarily, the IR absorption coefficient spectra of various p-type wafers are shown in Fig. 4. Note that the 150 µm sample with a fast ramp was not measured with FT-IR spectroscopy because of processing reasons.

The concentration of atomic hydrogen being bound in the various hydrogen complexes was calculated based on these measurements and is shown in Fig. 5. The LVMs of H_2 could not be detected in the thin, slowly cooled sample and neither were LVMs of phosphorus-hydrogen (PH) pairs in both n-type samples. The estimated detection limits are in the order of 10^{13} cm^{-3} for both H_2 molecules and PH pairs.

Looking at the p-type samples in Fig. 5, a clear trend can be observed from having very little hydrogen in the thin, slowly cooled sample to having two orders of magnitude more hydrogen in the thicker, faster cooled sample. Both 250 µm thick samples feature comparable amounts of hydrogen bound to boron, whereas the majority is bound in molecular form with the slow-cooled sample showing less [H_2].

Since the slow and fast processes feature a similar heating ramp (compare Fig. 2), we attribute the differences in [H_2] to the impact of the cooling ramp. Having a slower cooling ramp reduces the overall hydrogen content, but especially reduces [H_2] by more than 50%. The change toward the thin wafer is even greater. [H_2] is reduced by around two orders of magnitude and in [BH], a reduction by nearly one order of magnitude is observed.

However, these observations cannot be explained by a simple model, where hydrogen diffuses from the SiN_x layer into the bulk. In such a simple model, the driving force of the diffusion would be the concentration gradient between the SiN_x-layer and the bulk, with hydrogen concentrations differing several orders of magnitude. Considering a slower cooling rate, one would expect a larger hydrogen concentration present after a longer cooling phase. In thinner wafers, one would expect similar or even larger concentrations.

However, the experimental data show the opposite behavior, making the simple model improbable. They indicate that hydrogen not only diffuses into the bulk, but that out-diffusion also occurs during the cooling ramp—as already discussed in [68] or [69]. A possible reason could be differences in the temperature-dependent solubility between the silicon bulk and the passivation layers, which could lead to the passivation layers being a source or sink for hydrogen, depending on the temperature. Having a longer cool-down or thinner samples would then increase the hydrogen out-diffusion and thus lead to a smaller hydrogen concentration in the silicon bulk. However, the exact mechanism behind this and consequences such as the depth-wise distribution of hydrogen are still unclear and require further investigation.

The results in n-type show a similar trend. While all the detected hydrogen is found bound in its molecular form, a large out-diffusion of hydrogen appears to occur during the slower cool-down. Compared with the 250 µm p-type samples, the 200-µm n-type wafers show slightly different features: With a fast cooling ramp, a larger total [H] is observed, whereas the slower cooling leads to a lower total [H].

This implies that the specific kinetics of the hydrogen in- and out-diffusion might differ between p- and n-type wafers. Possible causes could, for example, be the charge state of atomic hydrogen and related diffusivities, or the trapping-kinetics of atomic hydrogen with the dopants, which all differ between B- and P-doped silicon [38], [51], [70], [71].

B. *Influencing the Extent of LeTID in p-Type Si*

In this section, we want to discuss how the different hydrogen configurations affect the extent of LeTID under LS at 77 ± 2 °C and 1 sun-equivalent illumination and DA at 175 ± 1 °C. We will focus only on the p-type wafers. Fig. 6 shows the maximum relative defect density $\beta_{\max}$ observed during the time series for LS and DA for the different p-type variations, as well as the initial concentration of BH pairs and H_2 molecules, measured with FT-IR spectroscopy. Additionally, the corresponding maximum

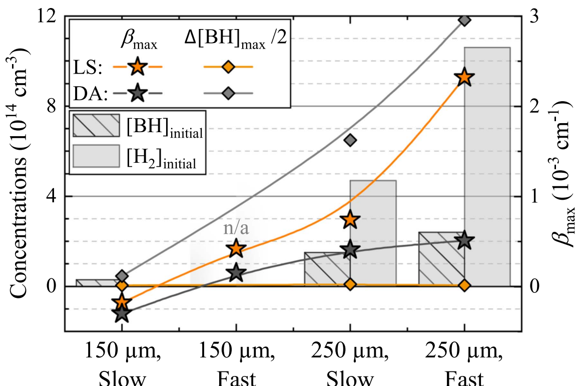

Fig. 6. Concentrations of BH pairs and H_2 molecules measured via FT-IR spectroscopy before degradation treatments are shown in bars (left *y*-axis) in the background. The maximum change in BH pair concentration during LS (orange) and DA (dark gray) is shown, too, with $\Delta[\mathrm{BH}]_{\max}$ divided by two for better visual comparison with $[H_2]$ (left *y*-axis). The maximum relative LeTID defect density $\beta_{\max}$ under LS and DA is shown, connected by b-splines (right *y*-axis). The negative values depict the impact of regeneration in samples without degradation. The corresponding temporal evolution of ΔN is shown in Fig. 7. No FT-IR and 4PP measurements could be conducted for the 150 µm, fast-cooled sample.

change in [BH] is depicted and divided by a factor of 2, since one H_2 molecule is expected to result in two BH pairs upon dissociation [compare (1) and (2)].

The LS data (orange) show a clear trend in maximum degradation extent between the four investigated samples. The fast-cooled 250 µm thick sample features the largest LeTID extent. A slower cooling reduces $\beta_{\max}$ by a factor of three and reducing the thickness while maintaining the fast cooling ramp leads to even less LeTID. The thin, slowly cooled sample shows no LeTID-related degradation at all, but instead a reduction in ΔN, indicated by the negative $\beta_{\max}$ in Fig. 6. We attribute this defect decrease to the regeneration of LeTID defects that are already present after firing (see Fig. 7 for the temporal evolution of ΔN).

Comparing this trend to the initially measured hydrogen concentrations, it seems that the LeTID extent scales with the concentration of molecular hydrogen H_2 in particular. This is especially pronounced in the large difference in H_2 and $\beta_{\max}$ between both 250 µm thick samples, as well as in the thin, slowly cooled sample that features no detectable $[H_2]$ and no detectable LeTID degradation.

During DA, a similar trend is observed: No degradation but a regeneration is seen in the 150 µm, slowly cooled sample, with the LeTID extent continuously increasing with thicker samples and a faster cooling ramp. Compared with $\beta_{\max}$ during LS, an overall lower LeTID extent is observed, which differs most significantly in the 250 µm fast-cooled sample.

Taking into account the change in [BH] pairs obtained from 4PP resistivity measurements, an opposite trend compared with the maximum LeTID extent $\beta_{\max}$ is observed: During LS no meaningful changes of [BH] are found, but during DA a clear trend can be observed with larger $[H_2]$ concentrations leading to larger $\Delta[\mathrm{BH}]_{\max}$. This is expected as under 175 °C DA conditions, H_2 is known to dissociate with the dissociated hydrogen forming BH pairs.

The observation can serve as an explanation for the difference in LeTID extent during LS and DA: based on the trend during LS, it is likely that $[H_2]$ is important for the formation of the LeTID defect. This results in a possible reaction where H_2 reacts with the LeTID precursor to form the LeTID defect. This could either occur by direct involvement of the molecule or indirectly by a dissociation of H_2 and subsequent association of atomic H with the LeTID precursor. During DA, a competing reaction to the LeTID reaction occurs with the formation of BH pairs. This reduces the amount of H_2 (or released atomic H) available for the LeTID reaction, thus reducing the overall LeTID extent, as can be seen in Fig. 6.

Please note that, interestingly, the maximum concentration of formed BH pairs exceeds the concentration expected from the FT-IR measured H_2 concentration ($\Delta[\mathrm{BH}]_{\max}/2 > [H_2]$). This may indicate an additional hydrogen source, but could also be because of potential systematic differences between FT-IR and resistivity measurements.

C. *Influencing the Kinetics of LeTID in p-Type Si*

The temporal evolution of the defect density during LS and DA is shown in Fig. 7. At first, an increase is observed that can be attributed to the formation of LeTID defects. The maximum defect density (I) is reached between 0.5 and 1 h under LS conditions and between 10 and 20 h during DA. Afterward, the defect density is reduced because of the regeneration up until a minimum (II) is reached. This decrease in ΔN is also visible in both thin, slowly cooled samples that show no LeTID degradation. Continuing the degradation treatment, another increase in the defect density is visible during DA, which can be attributed to the degradation of surface passivation (compare Section I-A). In our study, this surface-related degradation is only visible during DA. In contrast with results from [20], no SRD is visible during LS, even after more than one hundred hours of treatment. It needs to be mentioned that the wafers were stored for a couple of months in the dark after 5.5 h of LS until the treatment was continued. Whether or not this longer storage could be related to the absence of SRD is unclear, but its absence is in accordance with observations in [72].

Because the treatment under LS conditions is conducted under constant generation conditions ($\sim$1 sun-equivalent), Δn changes during degradation and regeneration with changing τ_{eff}. Since the LeTID kinetics are strongly influenced by the charge carrier density as, for example, discussed in [73], a reliable comparison can only be done for the case of DA.

As can be seen in Fig. 7, the temporal evolution differs between the samples. Apart from the thin, slowly cooled sample, we observe a remarkable difference in the time of maximum degradation, time of maximum regeneration, and the regeneration extent (i.e., the minimal measured defect density). The differences are depicted with black lines that indicate the degradation time at which the maximum (I) and minimum (II) occur. It is coherent to attribute these differences in temporal occurrences to differences in regeneration and surface degradation: Regeneration and surface degradation occur earlier, and the regeneration extent is larger if 1) the sample is cooled faster (compare both

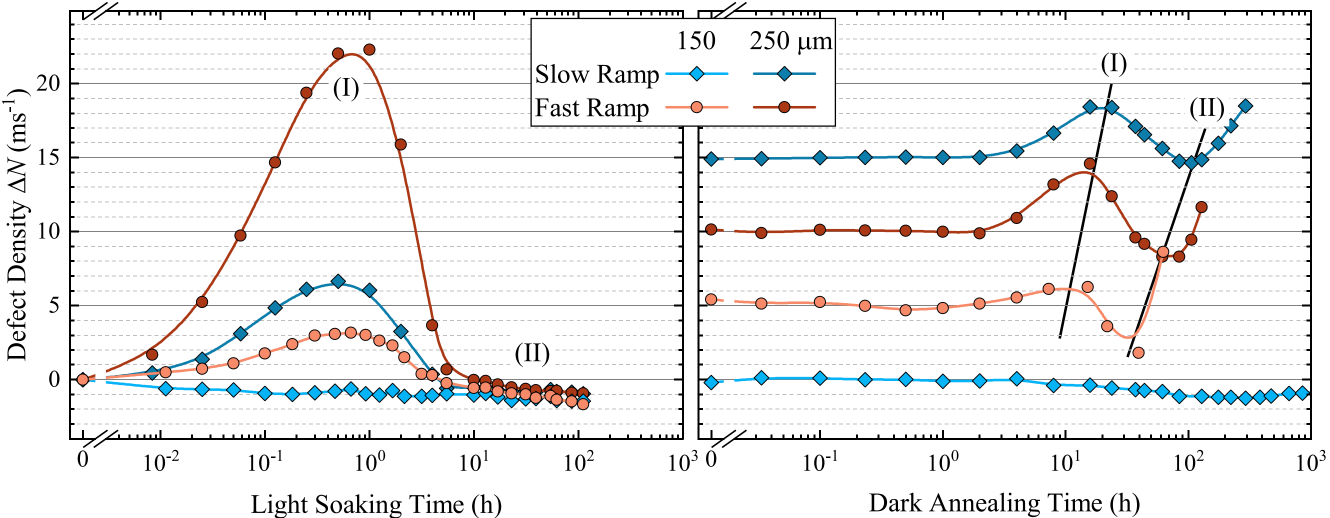

Fig. 7. Extracted lifetime-equivalent defect density ΔN of p-type samples during LS at 75 °C and ∼1 sun-equivalent (left) and DA at 175 °C (right). DA data are offset for better visual representation. Lines are b-splines serving as guide to the eyes. Additionally, the LeTID degradation maximum (I) and the minimum in ΔN due to regeneration (II) are depicted.

250 µm samples), and 2) the sample is thinner (compare both fast-cooled samples).

This behavior cannot be explained by the assumption that the reactions are only influenced by temperature. With photo-generated charge carriers also not playing a role, another reason must exist to describe the observed differences.

The chronological order of surface degradation always following LeTID regeneration has often been observed, and multiple authors speculated that both phenomena could be linked. An obvious hypothesis is that hydrogen moves toward the surface on longer timescales, inducing defects like hydrogen platelets [18], [21], [23], [74].

The results within this study support this idea: If the regeneration is driven by a diffusion of hydrogen toward the surface, having a shorter path toward the surface in a thinner sample would accelerate the regeneration and thus lead to an earlier onset of surface degradation. Within this model, the fast cooling ramp would not directly impact the kinetics, but it is rather likely that the hydrogen distribution into the wafer depth differs between the slow and fast ramp. We would expect that having a fast cooling ramp of 250 K/s will not give hydrogen enough time to distribute equally throughout the wafer. This would lead to an accumulation of hydrogen near the surface, thus accelerating the kinetics in a similar way a thinner wafer would do.

D. Comparing LeTID and Hydrogen Kinetics

To compare the individual kinetics of LeTID and hydrogen-related reactions, the defect density ΔN and the concentration of BH pairs are plotted in Fig. 8 for the 250 µm thick samples with a slow and fast cooling ramp.

Comparing LeTID and BH-kinetics, characteristic features in both dynamics are observed at similar times.

1) For the first two hours, no changes can be observed in ΔN and only a little increase in [BH] (until the first vertical line).

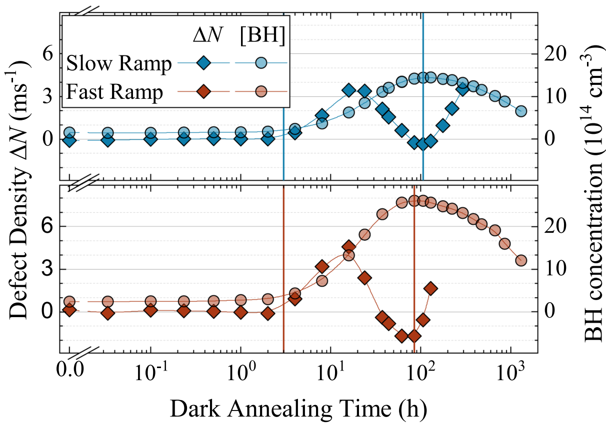

Fig. 8. Extracted lifetime-equivalent defect density ΔN and BH concentration shown for samples with 250 µm thickness and different cooling ramps during DA at 175 °C. Lines are b-splines serving as guide to the eyes, whereas vertical lines depict features at specific degradation times described in the text.

2) After two hours, an increase in [BH] is observed up to a maximum at around 100 h (second vertical line). During this time, the LeTID degradation and subsequent regeneration occur.
3) The minimum observed in ΔN coincides with the maximum of [BH]. Note that this feature occurs at different times for both samples (cf. discussion in Section III-C).
4) Afterward, we observe a decrease in [BH] and the simultaneous onset of surface degradation.

These temporal correlations have already been observed in [37] and suggest that there exists a connection between the lifetime-related changes and the hydrogen dynamics, which is discussed in the following.

Throughout the LeTID degradation and regeneration, atomic hydrogen is available because of the dissociation of H_2, as manifested in the atomic hydrogen binding to boron. As already

discussed in [37], in principle the following different reaction pathways could lead to LeTID degradation.

1) Atomic hydrogen dissociated from H_2 binds to the LeTID precursor and the LeTID defect is formed. For the regeneration, two processes are plausible: The dissociation of hydrogen from the LeTID defect, or the passivation of the defect, e.g., by another hydrogen atom.
2) H_2 could also directly bind to the LeTID precursor to form the defect. Here, the regeneration could be either the dissociation of one or both hydrogen atoms or the passivation of the defect, e.g., by hydrogen.
3) The LeTID precursor consists of hydrogen bound to the LeTID defect. During degradation, hydrogen dissociates from the precursor and leaves the recombination-active LeTID defect behind. The regeneration could be explained by a second dissociative reaction (e.g., the loss of a second H atom) or by a reconfiguration of the defect complex into a stable, recombination-inactive state.

In [37], we argued that the second theory is more likely based on considerations regarding the temporary recovery of the LeTID defect [52]. However, the new data in this study agrees much better with the first reaction, as explained in the following.

The first indication is the dependence of the LeTID extent on the H_2 content observed during LS and DA. The 150 µm thin, slowly cooled sample (compare Fig. 6) serves as a good example. With no detected H_2 molecules, no LeTID degradation is observed, which suggests that the presence of H_2 is needed to induce LeTID. In this line of thought, (atomic or molecular) hydrogen binds to the LeTID precursor in an association reaction to form the LeTID defect.

The LeTID kinetics during DA (cf. Fig. 7) indicate that the regeneration and surface degradation are likely related to a diffusion process toward the surface, as discussed above. With the surface providing a sink for hydrogen atoms, a concentration gradient develops over time that gives rise to a hydrogen flux toward the surface. In this picture, the LeTID precursor could be a stationary site within the host lattice that becomes recombination active if a hydrogen atom or molecule is captured. However, since hydrogen moves toward more stable complexes or the surface, it will eventually leave the precursor site and lead to the observed regeneration.

As can be seen in Fig. 8, the maximum in ΔN is reached before [BH] reaches its maximum, and the temporal evolution appears like ΔN could be related to the derivative of [BH] (until $[BH]_{max}$). The differences in temporal occurrence indicate that the LeTID defect acts as an intermediate state in the (simplified) reaction $H_2 \rightarrow$ LeTID defect $\rightarrow$ BH. As no changes in BH are detected during LS, this could indicate that the last reaction path might not occur during LS, but hydrogen diffuses toward the surface in another configuration—such as neutral H^0 stabilized by the presence of excess charge carriers. Under this assumption, the difference in the maximum relative defect density β_{max} between LS and DA indicates that most of the $H_2 \rightarrow BH$ reaction occurs without the LeTID intermediate state (compare Fig. 6 and discussion in Section III-B).

Which reactions dominate depends on the degradation conditions with the presence of excess charge carriers being of particular importance. This suggests that the charge states of the participants are important.

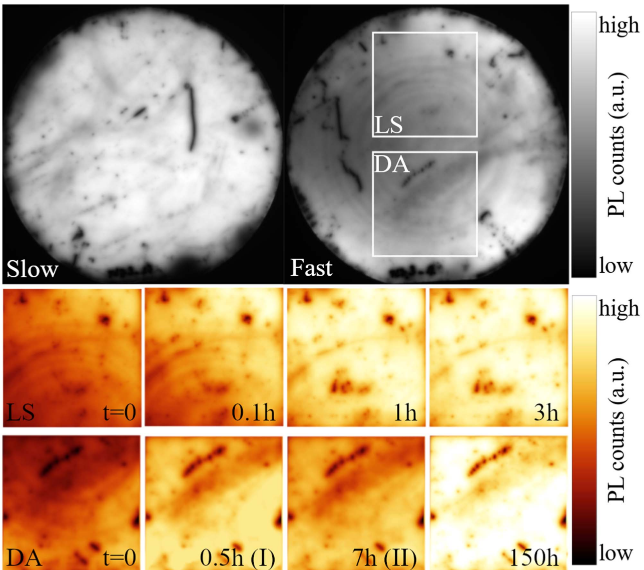

Fig. 9. PL images of n-type wafers after firing with a slow (top, left) and fast (top, right) cooling ramp, recorded with a generation of 1 sun-equivalent. The bottom two rows show sections of the PL images of the fast-cooled sample at different times during LS and DA. The roman numbers are references to specific times marked in Fig. 10. Each row features equal scaling. For the bottom two rows, a different color table is used to better visualize the striations.

At the surface, hydrogen forms a new complex that, again, leads to an increased recombination rate (surface degradation). As already speculated in [21] and [23], hydrogen platelets are a likely candidate. The formation of hydrogen platelets would be accompanied by a decrease in BH pairs and an increase in defect density, which would explain the characteristic features observed in Fig. 8 (second vertical line).

E. *LeTID in n-Type Si?*

The focus until now has been on the experimental results in p-type wafers where the issue of LeTID is more dominant. There are only a few studies of LeTID in n-type Si (e.g., [18], [75], and [76]). Its clear identification is hampered by the fact that defect-specific parameters like a k-factor of ~35 in p-type Si result in reduced recombination activity and a flat injection dependence of $\tau(\Delta n)$ in n-type, which is difficult to analyze.

As already presented in Section III-A (see Fig. 5), the hydrogen content in n-type is also significantly influenced by the cooling ramp of the fast-firing process, with slower cooling ramps reducing the H_2 concentration.

Besides the differences in hydrogen concentration, the different cooling ramps also impacted the effective lifetime of the n-type samples. The faster cooling ramp leads to a reduced overall τ_{eff}, but also to radial striations that can be seen in PL images, as shown in Fig. 9.

The evolution of the effective lifetime of those wafers during LS and DA is shown in Fig. 10. To evaluate whether the changes are related to bulk or surface phenomena, the full $\tau_{eff}(\Delta n)$ curve

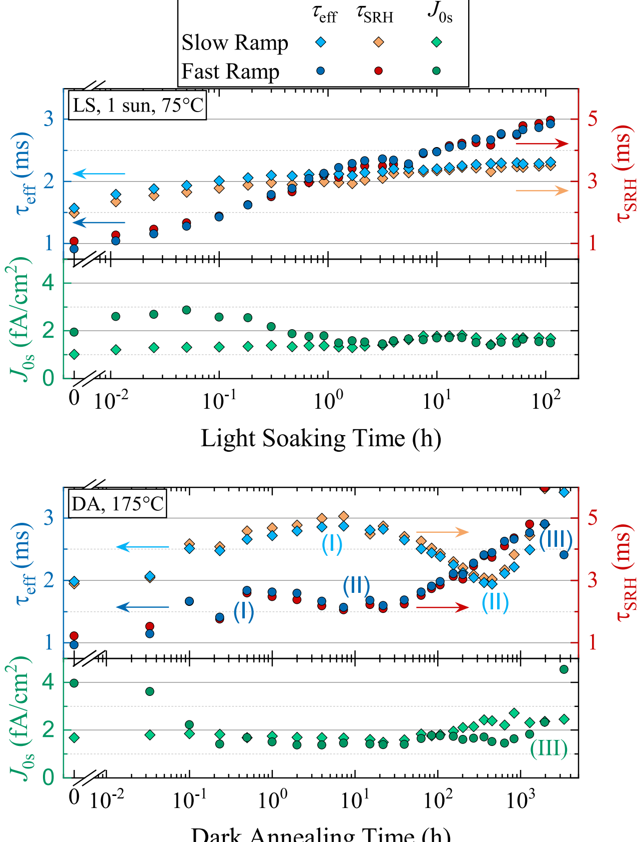

Fig. 10. Measured effective lifetime of 1 Ωcm n-type samples evaluated at $\Delta n = 1\cdot 10^{15}$ cm^{-3} during LS at 75 °C and ∼1 sun-equivalent (top) and DA at 175 °C (bottom). Samples with slower (faster) cooling ramp are depicted in light (dark) blue. Also shown are the results of full lifetime curve fits of the lifetime data obtained during LS and DA: τ_{SRH} is shown in orange (red) and J_{0s} in light (dark) green. Note the different scaling for τ_{eff} and τ_{SRH}.

is fitted between $\Delta n = 10^{15}$ and $2\cdot 10^{16}$ cm^{-3}. The fit is performed as using the latest intrinsic recombination models [77], [78], a τ_{SRH} with a flat Δn-dependence, and the surface recombination given in terms of the surface related recombination parameter J_{0s} using Sproul's approximation [79]. The only fit parameters are the bulk lifetime τ_{SRH} and J_{0s}, which are depicted in red and green.

During LS at the top of Fig. 10, the slow-cooled sample shows an increase in τ_{eff} until a plateau at around 2 ms is reached. The effective lifetime of the fast-cooled sample continuously increases, starting at a lower lifetime and ending at a higher lifetime compared with the slowly cooled sample. Looking at the fit results, the surface passivation remains constant throughout this treatment. Only a small change of J_{0s} is observed in the fast-cooled sample in the beginning, but its impact on τ_{eff} is minimal. Hence, the improvement of τ_{eff} is because of a decrease in bulk recombination, as can be observed from the corresponding behavior of τ_{SRH}. A very similar result is obtained for the case of DA, where most of the changes in τ_{eff} can be attributed to a change in bulk recombination rate.

It is also observed that during this initial τ_{eff} increase, the circular striations in the fast-cooled samples vanish (cf. Fig. 9). Similar circular striations have already been observed in p-type wafers that were LeTID degraded and were attributed to a (side) effect of LeTID [16], [75]. In [27], [75], and [80], a similar increase in τ_{eff} in n-type Si was observed, which was attributed to the regeneration of LeTID defects already present. The disappearance of the striations and the fact that it is a bulk-related phenomenon point in the same direction: It is likely that activated LeTID defects exist in n-type Si after firing and then regenerate during LS and DA.

The impact of the cooling ramp is similar to observations in p-type: fast-cooled samples reach similar (DA) or even higher (LS) lifetimes after regeneration compared with slow-cooled samples.

During DA, an additional minimum in τ_{eff} is observed (II) in the slow- and fast-cooled sample, which does not occur during LS. The lifetime analysis implies that this degradation-regeneration cycle can be attributed to a change in τ_{SRH} and hence LeTID, whereas J_{0s} stayed about constant throughout the experiment.

The first important hint supporting this hypothesis is that the lifetime minimum occurs at different times for the fast (∼7.3 h) and the slow (∼453 h) cooled sample. This follows the same trend observed in p-type Si (cf. right graph of Fig. 7). Second, the overall effects of DA and LS fit to what is observed in p-type Si. Fung et al. [81] and Sio et al. [28] showed that LS degraded p-type samples regenerate under DA but show a subsequent degradation-regeneration cycle, which would not occur if the samples were regenerated under LS conditions. A similar behavior is seen here: The (LeTID) degraded sample regenerates under LS and shows no further (bulk-related) degradation. During DA, however, the samples regenerate and then show a bulk-related degradation-regeneration cycle. From this, it can be hypothesized that the bulk-related degradation observed during DA (II) could be because of the additional formation of LeTID defects, which regenerate under subsequent treatment.

Surface degradation has been observed in n-type Si already, for example, in [22], [27], and [74]. Here, it is only observed in the fast-cooled sample during DA in the last data points, as seen in the increase in J_{0s} from 1.8 to 2.3 to 4.5 fA/cm^2. During LS, no SRD is observed, similar to the p-type samples (compare Fig. 7). However, as mentioned above, it is unclear whether this is a real effect or this is impacted by the same several-months-break after 5.5 h of total LS treatment time before the treatment was continued.

We expect that the slow-cooled sample will show SRD during DA at later degradation times. This behavior would be comparable to the p-type wafers (compare Fig. 7) and could hint at a similar cause.

IV. Conclusion

Within this study, we investigated how the cooling ramp of the fast-firing step and the wafer thickness affect the hydrogen configuration in p- and n-type silicon. We observed a lower total hydrogen content in thinner samples and samples with a slower cooling ramp. The difference in samples is especially pronounced in the hydrogen molecule concentration [H_2],

whereas the difference in BH pairs was comparably smaller. We hypothesize that the observed differences between samples are caused by an out-diffusion of hydrogen during the cooling ramp, with slower cooling ramps and thinner samples leading to a more significant out-diffusion of hydrogen.

We hypothesize that it is rather the amount of available H_2 than of BH pairs that is important for the maximum LeTID extent during LS and DA, with more H_2 leading to more LeTID defects. In particular, in a thin, slowly cooled sample, no significant amounts of H_2 could be detected with cryogenic FT-IR spectroscopy, which led to a LeTID-free sample under LS and DA.

In the n-type wafers, we observed the regeneration of a bulk-related defect (potentially LeTID) during LS and DA, as well as the additional formation of, presumably, LeTID defects during DA.

During DA of p-type wafers, we found a dependence of the regeneration and surface degradation rate on the sample thickness that indicates that both are related to a hydrogen-diffusion toward the surface. This is supported by an analysis of the formation and subsequent dissociation of BH pairs.

Combining all these findings, we postulate a potential sequence that can explain the LeTID degradation, regeneration, and surface degradation. A key element is the movement of hydrogen toward the surface. During this diffusion, hydrogen binds to the LeTID precursor within the host lattice leading to a recombination active defect. The regeneration of bulk lifetime is triggered by the dissociation of hydrogen from the LeTID defect complex. Once hydrogen reaches the surface, recombination active defects, like hydrogen platelets, are formed, leading to the observed surface degradation.

Acknowledgment

The authors would like to thank A. Leimenstoll, F. Schätzle, R. Neubauer, C. Harmel, D. Ourinson, S. Roder, and A. Nägele for help with sample processing and B. Steinhauser for providing the script to evaluate τ_{eff} curves.

References

[1] S. J. Pearton, J. W. Corbett, and T. S. Shi, “Hydrogen in crystalline semiconductors,” *Appl. Phys. A*, vol. 43, no. 3, pp. 153–195, 1987, doi: 10.1007/BF00615975.

[2] R. Lüdemann, “Hydrogen passivation of multicrystalline silicon solar cells,” *Mater. Sci. Eng., B*, vol. 58, no. 1/2, pp. 86–90, 1999, doi: 10.1016/S0921-5107(98)00288-8.

[3] S. Wilking, A. Herguth, and G. Hahn, “Influence of hydrogen on the regeneration of boron-oxygen related defects in crystalline silicon,” *J. Appl. Phys.*, vol. 113, no. 19, 2013, Art. no. 194503, doi: 10.1063/1.4804310.

[4] T. Niewelt, J. Schön, W. Warta, S. W. Glunz, and M. C. Schubert, “Degradation of crystalline silicon due to boron–oxygen defects,” *IEEE J. Photovolt.*, vol. 7, no. 1, pp. 383–398, Jan. 2017.

[5] K. Ramspeck et al., “Light induced degradation of rear passivated mc-Si solar cells,” in *Proc. 27th Eur. Photovolt. Sol. Energy Conf. Exhib.*, 2012, vol. 1, pp. 861–865, doi: 10.4229/27THEUPVSEC2012-2DO.3.4.

[6] T. Niewelt et al., “Understanding the light-induced degradation at elevated temperatures: Similarities between multicrystalline and floatzone p-type silicon,” *Prog. Photovolt. Res. Appl.*, vol. 26, no. 8, pp. 533–542, 2018, doi: 10.1002/pip.2954.

[7] C. Vargas et al., “Carrier-induced degradation in multicrystalline silicon: Dependence on the silicon nitride passivation layer and hydrogen released during firing,” *IEEE J. Photovolt.*, vol. 8, no. 2, pp. 413–420, Mar. 2018.

[8] M. A. Jensen et al., “Evaluating root cause: The distinct roles of hydrogen and firing in activating light- and elevated temperature-induced degradation,” *J. Appl. Phys.*, vol. 124, no. 8, 2018, Art. no. 085701, doi: 10.1063/1.5041756.

[9] F. Kersten et al., “Degradation of multicrystalline silicon solar cells and modules after illumination at elevated temperature,” *Sol. Energy Mater. Sol. Cells*, vol. 142, pp. 83–86, 2015, doi: 10.1016/j.solmat.2015.06.015.

[10] P. P. Altermatt et al., “Requirements of the Paris Climate Agreement for the coming 10 years on investments, technical roadmap, and expansion of PV manufacturing,” in *Proc. 37th Eur. Photovolt. Sol. Energy Conf. Exhib.*, 2020, pp. 1999–2004, doi: 10.4229/EUPVSEC20202020-7CP.1.2.

[11] J.-I. Polzin et al., “Thermal activation of hydrogen for defect passivation in poly-Si based passivating contacts,” *Sol. Energy Mater. Sol. Cells*, vol. 230, 2021, Art. no. 111267, doi: 10.1016/j.solmat.2021.111267.

[12] R. Eberle, W. Kwapil, F. Schindler, M. C. Schubert, and S. W. Glunz, “Impact of the firing temperature profile on light induced degradation of multicrystalline silicon,” *Phys. Status Solidi–Rapid Res. Lett.*, vol. 10, no. 12, pp. 861–865, 2016, doi: 10.1002/pssr.201600272.

[13] U. Varshney et al., “Impact of substrate thickness on the degradation in multicrystalline silicon,” *IEEE J. Photovolt.*, vol. 11, no. 1, pp. 65–72, Jan. 2021.

[14] H. C. Sio et al., “Light and elevated temperature induced degradation in p-type and n-type cast-grown multicrystalline and mono-like silicon,” *Sol. Energy Mater. Sol. Cells*, vol. 182, pp. 98–104, 2018, doi: 10.1016/j.solmat.2018.03.002.

[15] D. Chen et al., “Evidence of an identical firing-activated carrier-induced defect in monocrystalline and multicrystalline silicon,” *Sol. Energy Mater. Sol. Cells*, vol. 172, pp. 293–300, 2017, doi: 10.1016/j.solmat.2017.08.003.

[16] T. Niewelt et al., “Light-induced activation and deactivation of bulk defects in boron-doped float-zone silicon,” *J. Appl. Phys.*, vol. 121, no. 18, 2017, Art. no. 185702, doi: 10.1063/1.4983024.

[17] D. Sperber, A. Herguth, and G. Hahn, “Investigating possible causes of light induced degradation in boron-doped float-zone silicon,” in *Proc. Eur. Photovolt. Sol. Energy Conf. Exhib.*, 2017, pp. 565–568, doi: 10.4229/EU-PVSEC20172017-2AV.1.39.

[18] D. Chen et al., “Hydrogen induced degradation: A possible mechanism for light- and elevated temperature-induced degradation in n-type silicon,” *Sol. Energy Mater. Sol. Cells*, vol. 185, pp. 174–182, 2018, doi: 10.1016/j.solmat.2018.05.034.

[19] W. Kwapil, J. Dalke, R. Post, and T. Niewelt, “Influence of dopant elements on degradation phenomena in B- and Ga-doped Czochralski-grown silicon,” *Sol. RRL*, vol. 5, 2021, Art. no. 2100147, doi: 10.1002/solr.202100147.

[20] D. Sperber, A. Graf, D. Skorka, A. Herguth, and G. Hahn, “Degradation of surface passivation on crystalline silicon and its impact on light-induced degradation experiments,” *IEEE J. Photovolt.*, vol. 7, no. 6, pp. 1627–1634, Nov. 2017.

[21] K. Kim et al., “Degradation of surface passivation and bulk in p-type monocrystalline silicon wafers at elevated temperature,” *IEEE J. Photovolt.*, vol. 9, no. 1, pp. 97–105, Jan. 2019.

[22] D. Chen et al., “Hydrogen-induced degradation: Explaining the mechanism behind light- and elevated temperature-induced degradation in n- and p-type silicon,” *Sol. Energy Mater. Sol. Cells*, vol. 207, 2020, Art. no. 110353, doi: 10.1016/j.solmat.2019.110353.

[23] P. Hamer, D. Chen, and R. S. Bonilla, “Thermal processes and their impact on surface-related degradation,” *Physica Status Solidi–Rapid Res. Lett.*, vol. 16, 2021, Art. no. 2100464, doi: 10.1002/pssr.202100464.

[24] C. E. Chan et al., “Rapid stabilization of high-performance multicrystalline P-type silicon PERC cells,” *IEEE J. Photovolt.*, vol. 6, no. 6, pp. 1473–1479, Nov. 2016.

[25] F. Maischner et al., “LeTID mitigation via an adapted firing process in p-type PERC cells from SMART cast-monocrystalline, Czochralski and high-performance multicrystalline silicon,” *Prog. Photovolt. Res. Appl.*, vol. 30, no. 2, pp. 123–131, 2021, doi: 10.1002/pip.3467.

[26] C. Chan et al., “Modulation of carrier-induced defect kinetics in multicrystalline silicon PERC cells through dark annealing,” *Sol. RRL*, vol. 1, no. 2, 2017, Art. no. 1600028, doi: 10.1002/solr.201600028.

[27] B. Hammann, J. Engelhardt, D. Sperber, A. Herguth, and G. Hahn, “Influencing light and elevated temperature induced degradation and surface-related degradation kinetics in float-zone silicon by varying the initial sample state,” *IEEE J. Photovolt.*, vol. 10, no. 1, pp. 85–93, Jan. 2020.

[28] H. C. Sio et al., “The role of dark annealing in light and elevated temperature induced degradation in p-type mono-like silicon,” *IEEE J. Photovolt.*, vol. 10, no. 4, pp. 992–1000, Jul. 2020.

[29] U. Varshney et al., "Evaluating the impact of SiN_x thickness on lifetime degradation in silicon," *IEEE J. Photovolt.*, vol. 9, no. 3, pp. 601–607, May 2019.

[30] J. Lindroos, A. Zuschlag, D. Skorka, and G. Hahn, "Silicon nitride deposition: Impact on lifetime and light-induced degradation at elevated temperature in multicrystalline silicon," *IEEE J. Photovolt.*, vol. 10, no. 1, pp. 8–18, Jan. 2020.

[31] U. Varshney et al., "Controlling light- and elevated-temperature-induced degradation with thin film barrier layers," *IEEE J. Photovolt.*, vol. 10, no. 1, pp. 19–27, Jan. 2020.

[32] A. Schmid et al., "On the role of AlO_x thickness in AlO_x/SiN_y:H layer stacks regarding light- and elevated temperature-induced degradation and hydrogen diffusion in c-Si," *IEEE J. Photovolt.*, vol. 11, no. 4, pp. 967–973, Jul. 2021.

[33] D. Bredemeier, D. C. Walter, and J. Schmidt, "Possible candidates for impurities in mc-Si wafers responsible for light-induced lifetime degradation and regeneration," *Sol. RRL*, vol. 2, no. 1, 2018, Art. no. 1700159, doi: 10.1002/solr.201700159.

[34] J. Schmidt, D. Bredemeier, and D. C. Walter, "On the defect physics behind light and elevated temperature-induced degradation (LeTID) of multicrystalline silicon solar cells," *IEEE J. Photovolt.*, vol. 9, no. 6, pp. 1497–1503, Nov. 2019.

[35] D. Bredemeier, D. C. Walter, R. Heller, and J. Schmidt, "Impact of hydrogen-rich silicon nitride material properties on light-induced lifetime degradation in multicrystalline silicon," *Phys. Status Solidi–Rapid Res. Lett.*, vol. 13, no. 8, 2019, Art. no. 1900201, doi: 10.1002/pssr.201900201.

[36] L. Helmich, D. C. Walter, D. Bredemeier, and J. Schmidt, "Atomic-layer-deposited Al_2O_3 as effective barrier against the diffusion of hydrogen from SiN_x:H layers into crystalline silicon during rapid thermal annealing," *Phys. Status Solidi–Rapid Res. Lett.*, vol. 14, 2020, Art. no. 2000367, doi: 10.1002/pssr.202000367.

[37] B. Hammann, L. Rachdi, W. Kwapil, F. Schindler, and M. C. Schubert, "Insights into the hydrogen-related mechanism behind defect formation during light- and elevated-temperature-induced degradation," *Physica Status Solidi–Rapid Res. Lett.*, vol. 15, no. 6, 2021, Art. no. 2000584, doi: 10.1002/pssr.202000584.

[38] C. Sun, D. Yan, and D. Macdonald, "Modeling the charge state of monatomic hydrogen and other defects with arbitrary concentrations in crystalline silicon," *Physica Status Solidi–Rapid Res. Lett.*, vol. 15, no. 11, 2021, Art. no. 2100483, doi: 10.1002/pssr.202100483.

[39] I. L. Kolevatov, P. M. Weiser, E. V. Monakhov, and B. G. Svensson, "Interaction between hydrogen and vacancy defects in crystalline silicon," *Phys. Status Solidi A*, vol. 216, no. 10, 2019, Art. no. 1800670, doi: 10.1002/pssa.201800670.

[40] C.-T. Sah, J. Y.-C. Sun, and J. J.-T. Tzou, "Deactivation of the boron acceptor in silicon by hydrogen," *Appl. Phys. Lett.*, vol. 43, no. 2, pp. 204–206, 1983, doi: 10.1063/1.94287.

[41] S. Bergman, S. J. Pearton, and J. Lopata, "Donor-hydrogen complexes in passivated silicon," *Phys. Rev. B, Condens. Matter*, vol. 37, no. 5, pp. 2770–2773, 1988, doi: 10.1103/physrevb.37.2770.

[42] T. Zundel and J. Weber, "Boron reactivation kinetics in hydrogenated silicon after annealing in the dark or under illumination," *Phys. Rev. B, Condens. Matter*, vol. 43, no. 5, pp. 4361–4372, 1991, doi: 10.1103/physrevb.43.4361.

[43] T. Zundel and J. Weber, "Trap-limited hydrogen diffusion in boron-doped silicon," *Phys. Rev. B, Condens. Matter*, vol. 46, no. 4, pp. 2071–2077, 1992, doi: 10.1103/physrevb.46.2071.

[44] D. C. Walter, D. Bredemeier, R. Falster, V. V. Voronkov, and J. Schmidt, "Easy-to-apply methodology to measure the hydrogen concentration in boron-doped crystalline silicon," *Sol. Energy Mater. Sol. Cells*, vol. 200, 2019, Art. no. 109970, doi: 10.1016/j.solmat.2019.109970.

[45] C. Winter, J. Simon, and A. Herguth, "Study on boron–hydrogen pairs in bare and passivated float-zone silicon wafers," *Phys. Status Solidi A*, vol. 218, no. 23, 2021, Art. no. 2100220, doi: 10.1002/pssa.202100220.

[46] Y. Acker, J. Simon, and A. Herguth, "Formation dynamics of BH and GaH-pairs in crystalline silicon during dark annealing," *Phys. Status Solidi A*, vol. 219, 2022, Art. no. 2200142, doi: 10.1002/pssa.202200142.

[47] N. Fukata et al., "Formation of hydrogen-boron complexes in boron-doped silicon treated with a high concentration of hydrogen atoms," *Phys. Rev. B*, vol. 72, no. 24, 2005, Art. no. 245209, doi: 10.1103/PhysRevB.72.245209.

[48] R. E. Pritchard, J. H. Tucker, R. C. Newman, and E. C. Lightowlers, "Hydrogen molecules in boron-doped crystalline silicon," *Semicond. Sci. Technol.*, vol. 14, no. 1, pp. 77–80, 1999, doi: 10.1088/0268-1242/14/1/011.

[49] P. M. Weiser, E. Monakhov, H. Haug, M. S. Wiig, and R. Søndenå, "Hydrogen-related defects measured by infrared spectroscopy in multicrystalline silicon wafers throughout an illuminated annealing process," *J. Appl. Phys.*, vol. 127, no. 6, 2020, Art. no. 065703, doi: 10.1063/1.5142476.

[50] V. V. Voronkov and R. Falster, "Formation, dissociation, and diffusion of various hydrogen dimers in silicon," *Phys. Status Solidi B*, vol. 254, no. 6, 2017, Art. no. 1600779, doi: 10.1002/pssb.201600779.

[51] P. Hamer et al., "Modelling of hydrogen transport in silicon solar cell structures under equilibrium conditions," *J. Appl. Phys.*, vol. 123, no. 4, 2018, Art. no. 043108, doi: 10.1063/1.5016854.

[52] W. Kwapil, J. Schon, T. Niewelt, and M. C. Schubert, "Temporary recovery of the defect responsible for light- and elevated temperature-induced degradation: Insights into the physical mechanisms behind LeTID," *IEEE J. Photovolt.*, vol. 10, no. 6, pp. 1591–1603, Nov. 2020.

[53] M. J. Binns, R. C. Newman, S. A. McQuaid, and E. C. Lightowlers, "Hydrogen solubility and defects in silicon," *Mater. Sci. Forum*, vol. 143–147, pp. 861–866, 1993, doi: 10.4028/www.scientific.net/MSF.143-147.861.

[54] D. C. Walter, V. V. Voronkov, R. Falster, D. Bredemeier, and J. Schmidt, "On the kinetics of the exchange of hydrogen between hydrogen–boron pairs and hydrogen dimers in crystalline silicon," *J. Appl. Phys.*, vol. 131, no. 16, 2022, Art. no. 165702, doi: 10.1063/5.0086307.

[55] N. E. Grant et al., "Thermal activation and deactivation of grown-in defects limiting the lifetime of float-zone silicon," *Phys. Status Solidi–Rapid Res. Lett.*, vol. 10, no. 6, pp. 443–447, 2016, doi: 10.1002/pssr.201600080.

[56] S. Roder, T. Niewelt, A. Brand, J. Schneider, and J. Nekarda, "Temperature gradient image analysis to optimize an ultrafast regeneration of boron–oxygen-related defects," *IEEE J. Photovolt.*, vol. 11, no. 3, pp. 606–612, May 2021.

[57] O. John et al., "Laser metal bonding (LMB)—Low impact joining of thin aluminum foil to silicon and silicon nitride surfaces," *Proc. CIRP*, vol. 94, pp. 863–868, 2020, doi: 10.1016/j.procir.2020.09.109.

[58] A. Herguth and C. Winter, "Methodology and error analysis of direct resistance measurements used for the quantification of boron–hydrogen pairs in crystalline silicon," *IEEE J. Photovolt.*, vol. 11, no. 4, pp. 1059–1068, Jul. 2021.

[59] S. A. McQuaid et al., "Concentration of atomic hydrogen diffused into silicon in the temperature range 900–1300 °C," *Appl. Phys. Lett.*, vol. 58, no. 25, pp. 2933–2935, 1991, doi: 10.1063/1.104726.

[60] R. E. Pritchard et al., "Interactions of hydrogen molecules with bond-centered interstitial oxygen and another defect center in silicon," *Phys. Rev.. B, Condens. Matter*, vol. 56, no. 20, pp. 13118–13125, 1997, doi: 10.1103/PhysRevB.56.13118.

[61] A. Fell, J. Schön, M. C. Schubert, and S. W. Glunz, "The concept of skins for silicon solar cell modeling," *Sol. Energy Mater. Sol. Cells*, vol. 173, pp. 128–133, 2017, doi: 10.1016/j.solmat.2017.05.012.

[62] A. Fell, "Quokka3," [Online]. Available: https://www.quokka3.com

[63] R. A. Sinton and A. Cuevas, "Contactless determination of current–voltage characteristics and minority-carrier lifetimes in semiconductors from quasi-steady-state photoconductance data," *Appl. Phys. Lett.*, vol. 69, no. 17, pp. 2510–2512, 1996, doi: 10.1063/1.117723.

[64] J. A. Giesecke, M. C. Schubert, B. Michl, F. Schindler, and W. Warta, "Minority carrier lifetime imaging of silicon wafers calibrated by quasi-steady-state photoluminescence," *Sol. Energy Mater. Sol. Cells*, vol. 95, no. 3, pp. 1011–1018, 2011, doi: 10.1016/j.solmat.2010.12.016.

[65] A. Herguth, "On the lifetime-equivalent defect density: Properties, application, and pitfalls," *IEEE J. Photovolt.*, vol. 9, no. 5, pp. 1182–1194, Sep. 2019.

[66] M. Kim et al., "Defect concentration and δn change in light- and elevated temperature-induced degradation," *J. Phys. D, Appl. Phys.*, vol. 55, no. 8, 2022, Art. no. 085106, doi: 10.1088/1361-6463/ac34a8.

[67] D. Sperber, F. Furtwängler, A. Herguth, and G. Hahn, "Does LeTID occur in c-Si even without a firing step?," *AIP Conf. Proc.*, vol. 2147, no. 1, 2019, Art. no. 140011, doi: 10.1063/1.5123898.

[68] S. Wilking, S. Ebert, A. Herguth, and G. Hahn, "Influence of hydrogen effusion from hydrogenated silicon nitride layers on the regeneration of boron–oxygen related defects in crystalline silicon," *J. Appl. Phys.*, vol. 114, no. 19, 2013, Art. 194512, doi: 10.1063/1.4833243.

[69] S. H. Lee, M. F. Bhopal, D. W. Lee, and S. H. Lee, "Review of advanced hydrogen passivation for high efficient crystalline silicon solar cells," *Mater. Sci. Semicond. Process.*, vol. 79, pp. 66–73, 2018, doi: 10.1016/j.mssp.2018.01.019.

[70] B. J. Hallam et al., “Development of advanced hydrogenation processes for silicon solar cells via an improved understanding of the behaviour of hydrogen in silicon,” *Prog. Photovolt. Res. Appl.*, vol. 28, no. 12, pp. 1217–1238, 2020, doi: 10.1002/pip.3240.

[71] D. Gomes, V. P. Markevich, A. R. Peaker, and J. Coutinho, “Dynamics of hydrogen in silicon at finite temperatures from first principles,” *Phys. Status Solidi B*, vol. 259, 2022, Art. no. 2100670, doi: 10.1002/pssb.202100670.

[72] T. Niewelt, W. Kwapil, M. Selinger, A. Richter, and M. C. Schubert, “Stability of effective lifetime of float-zone silicon wafers with AlO_x surface passivation schemes under illumination at elevated temperature,” *Energy Proc.*, vol. 124, pp. 146–151, 2017, doi: 10.1016/j.egypro.2017.09.320.

[73] W. Kwapil, T. Niewelt, and M. C. Schubert, “Kinetics of carrier-induced degradation at elevated temperature in multicrystalline silicon solar cells,” *Sol. Energy Mater. Sol. Cells*, vol. 173, pp. 80–84, 2017, doi: 10.1016/j.solmat.2017.05.066.

[74] D. Sperber, A. Schwarz, A. Herguth, and G. Hahn, “Enhanced stability of passivation quality on diffused silicon surfaces under light-induced degradation conditions,” *Sol. Energy Mater. Sol. Cells*, vol. 188, pp. 112–118, 2018, doi: 10.1016/j.solmat.2018.08.019.

[75] T. Niewelt, R. Post, F. Schindler, W. Kwapil, and M. C. Schubert, “Investigation of LeTID where we can control it—Application of FZ silicon for defect studies,” in *Proc. 15th Int. Conf. Concentrator Photovolt. Syst.*, Fes, Morocco, 2019, Art. no. 140006, doi: 10.1063/1.5123893.

[76] C. Vargas et al., “Degradation and recovery of n-type multi-crystalline silicon under illuminated and dark annealing conditions at moderate temperatures,” *IEEE J. Photovolt.*, vol. 9, no. 2, pp. 355–363, Mar. 2019.

[77] T. Niewelt et al., “Reassessment of the intrinsic bulk recombination in crystalline silicon,” *Sol. Energy Mater. Sol. Cells*, vol. 235, 2022, Art. no. 111467, doi: 10.1016/j.solmat.2021.111467.

[78] A. Fell et al., “Radiative recombination in silicon photovoltaics: Modeling the influence of charge carrier densities and photon recycling,” *Sol. Energy Mater. Sol. Cells*, vol. 230, 2021, Art. no. 111198, doi: 10.1016/j.solmat.2021.111198.

[79] A. B. Sproul, “Dimensionless solution of the equation describing the effect of surface recombination on carrier decay in semiconductors,” *J. Appl. Phys.*, vol. 76, no. 5, pp. 2851–2854, 1994, doi: 10.1063/1.357521.

[80] D. Sperber, A. Graf, A. Heilemann, A. Herguth, and G. Hahn, “Bulk and surface instabilities in boron doped float-zone samples during light induced degradation treatments,” *Energy Proc.*, vol. 124, pp. 794–798, 2017, doi: 10.1016/j.egypro.2017.09.349.

[81] T. H. Fung et al., “A four-state kinetic model for the carrier-induced degradation in multicrystalline silicon: Introducing the reservoir state,” *Sol. Energy Mater. Sol. Cells*, vol. 184, pp. 48–56, 2018, doi: 10.1016/j.solmat.2018.04.024.